Journal of Catalysis 366 (2018) 50–60

Contents lists available at ScienceDirect

Journal of Catalysis

journal homepage: www.elsevier.com/locate/jcat

Tuning the activity/stability balance of anion doped CoS_xSe_{2-x} dichalcogenides

Y. Li [a], T. Polakovic [b], J. Curtis [b], S.L. Shumlas [c], S. Chatterjee [a], S. Intikhab [a], D.A. Chareev [d,e,h], O.S. Volkova [d,f,g], A.N. Vasiliev [d,f,g], G. Karapetrov [b], J. Snyder [a,*]

[a] Department of Chemical and Biological Engineering, Drexel University, Philadelphia, PA 19104, United States
[b] Department of Physics, Drexel University, Philadelphia, PA 19104, United States
[c] Department of Chemistry, Temple University, Philadelphia, PA 19122, United States
[d] Ural Federal University, 620002 Ekaterinburg, Russia
[e] Institute of Experimental Mineralogy, RAS, 142432 Chernogolovka, Russia
[f] Low Temperature Physics and Superconductivity Department, Physics Faculty, M. V. Lomonosov Moscow State University, Moscow 119991, Russia
[g] National University of Science and Technology MISiS, Moscow 119049, Russia
[h] Institute of Geology and Petroleum Technologies, Kazan Federal University, Kazan, Russia

ARTICLE INFO

Article history:
Received 23 April 2018
Revised 20 July 2018
Accepted 23 July 2018
Available online 13 August 2018

Keywords:
Transition metal dichalcogenides
Hydrogen evolution reaction
Anion doping
Electrocatalysis

ABSTRACT

We present a thorough assessment of the compositional dependent hydrogen evolution reaction (HER) activity and stability for Co-based mixed chalcogen, CoS_xSe_{2-x}, transition metal dichalcogenides (TMDs). In direct contrast to other reports on mixed chalcogen TMDs that have been limited to Mo and W, we observe a decrease in HER activity for any departure from the pure, single chalcogen composition, CoS_2 and $CoSe_2$. The single chalcogen TMDs are found to have nearly identical HER activity. Bulk resistivity of the pure and mixed chalcogen TMDs as well as the charge transfer resistance for the HER are found to be most optimal for $CoSe_2$. However, $CoSe_2$ is predicted to have an endothermic hydrogen adsorption free energy in contrast to the slightly exothermic hydrogen adsorption free energy for CoS_2. This highlights the convolution of hydrogen adsorption free energy and material conductivity in determining the HER activity for even metallic conducting TMDs. Sulfur-rich Co-based TMDs with a pyrite-type crystal structure are found to quickly deactivate through loss of Co and formation of passivating reduced sulfur species at the surface while Se-rich compositions are observed to be more stable. Therefore, with an HER activity matching that of CoS_2, but with a dramatic improvement in stability, $CoSe_2$ breaks away from the traditional inverse activity – stability relationship and represents a promising non-PGM HER electrocatalyst for acidic PEM electrolyzers.

1. Introduction

The future of renewable energy centers on the advancement of technologies that will bridge the gap between peak energy production and peak energy demand as well as readily make the transition from stationary to portable power. Storing the energy produced from intermittent renewable sources in the form of chemical bonds shows great promise for both stationary and transportation applications. Hydrogen represents one of the simplest forms of electrochemical fuels. With a high gravimetric energy density (120 MJ/kg) [1] and sourced from water, hydrogen is an ideal energy storage fuel, operating outside of the carbon cycle. Polymer electrolyte membrane (PEM) electrolysis is an advanced, commercialized technology for the generation of H_2 from H_2O; however, both the cathode (H_2 side) and anode (O_2 side) electrodes are loaded with precious metal based catalysts, typically Pt on the cathode and Ru and/or Ir oxides on the anode [2–4]. The expense and limited availability of these catalytic materials puts a significant constraint on the wide-spread adoption of electrochemical fuel generation technologies. The task then becomes finding an earth-abundant material that has comparable activity and stability to the requisite precious metal based catalysts.

Sulfur-based transition metal dichalcogenides (TMDs) have emerged as a promising alternative to platinum group metal (PGM) hydrogen evolution reaction (HER) electrocatalysts as they are abundant, inexpensive, and exhibit a low HER overpotential with surprising stability in acidic electrolytes, pH $\leqslant$ 1 [5–13]. Naturally occurring enzymes including hydrogenases and nitrogenases efficiently split water at sulfur coordinated Mo and Ni/Fe

* Corresponding author.
E-mail address: jds43@drexel.edu (J. Snyder).

https://doi.org/10.1016/j.jcat.2018.07.030
0021-9517/

metal centers [13,14]. TMDs closely mimic the active site geometry and coordination structure of these enzymes with molybdenum disulfide (MoS_2), a common hydrodesulfurization catalyst [7,12,15], emerging as the standard for TMD HER electrocatalysts [5,6,8,9,12,15–26]. Initial studies of well-defined MoS_2 thin films identified the edges as active sites while the basal planes were determined to be inactive [12]. Subsequent computational analysis of the HER reaction on two-dimensional TMDs has quantified the adsorption free energy of atomic hydrogen (ΔG_{Had}) on different edge/basal structures and compositions, corroborating the experimental results while giving important insight for further optimization [9,12,15,20,22,24,25,27]. The adsorbed hydrogen intermediate is found to have the most optimal ΔG_{Had}, closest to thermoneutral, at the S-edge of the MoS_2 2D structure [15,20,22,28]. The edges of 2D MoS_2 are also found to have metallic electronic character [7,8,12,15,17,19,24,29], while MoS_2 itself is a semiconducting material [12,21,29]. The HER overpotential for bulk MoS_2 is prohibitively high and only after directed nanostructuring of MoS_2 to preferentially expose the active edge sites is an appreciable activity obtained [5,6,9,12,18,19,21,30,31].

Since the first reports of the high intrinsic activity of the edge sites of 2D MoS_2 [12], significant effort has been centered on optimizing nanoscale geometry to expose the highest density of edge sites and maximize activity [5,6,9,16–19,21,32–35]. Further optimization of TMD HER activity has been achieved through the addition of transition metal (cation) dopants into the TMD lattice [20,25,31]. Transition metal dopant species incorporated in the edge of MoS_2 were found to shift the ΔG_{Had} on both the Mo-edge and S-edge. The S-edge of the doped TMDs is predicted to exhibit similar HER activity to the Mo-edge of undoped TMDs [20,25]. For single metal 2D TMDs, the hydrogen adsorption strength is calculated to be prohibitively weak on the S-edge. As the S-edge makes up nearly half of the exposed surface in 2D TMDs [20], an optimization of the H-binding on the S-edge effectively increases the active site density and thus the catalytic activity. For many TMDs, the impact of doping with a second chalcogen (anion) on the electronic structure is found to be small in comparison to cation doping [7,6]. However, in seeming contradiction to the theoretical calculations relying on ΔG_{Had} as the singular activity descriptor, recent work assessing the impact of anion doping, either in the form of $MS_{(x)}X_{(2-x)}$ [36,37] (X = Se, Te) or through heterostructures with a high interfacial area between MS_2 and MX_2 rich phases [38,39], have demonstrated significant improvements in the HER activity. These observed HER activity enhancements have been noted for W [38] and Mo [36,37] based TMDs where in each case the highest activity was found for the mixed chalcogen compositions. The origin of this activity enhancement has been attributed to several potential sources: (1) the introduction of a second chalcogen atom into the TMD lattice causes a strain at the surface, modifying the geometric and electronic structure and optimizing ΔG_{Had}; (2) evolution of a high interfacial area between MS_2-rich and MX_2-rich phases through phase separation, optimizing ΔG_{Had}; or (3) anion doping induced changes to the TMD atomic geometry, shifting it from semiconducting, which is the dominant electronic behavior of both MoX_2 and WX_2 [5,8,9,12,15,17,18,40], to metallic and thus improving the charge transfer through the catalyst.

While only the low-coordinated sulfur atoms on the Mo-edge of exfoliated 2D-MoS_2 are active for the HER due to the low conductivity and weak adsorption of atomic hydrogen on the basal planes, pyrite-group TMDs, including CoS_2 and $CoSe_2$, are HER active in their bulk form due to their intrinsic metallic-like conductivity [11,13,30,40–44]. The CoS_xSe_{2-x} pyrite-type cubic crystal structure (No. 205, $T_h^6, Pa\bar{3}$) is closely related to that of NaCl (No. 225, $O_h^5, Fm\bar{3}m$), with Co atoms at the face-centered positions of Na sites and centers of S_2/Se_2 dumbbells at the Cl sites. These dumbbells are oriented along the ⟨1 1 1⟩ directions in the unit cell, with each unit cell containing four $CoS_2(Se_2)$ molecules. Each Co atom is surrounded by six chalcogen atoms forming a trigonally distorted octahedron, where each chalcogen links to three Co atoms and a single other chalcogen atom, forming a distorted tetrahedral structure [45]. The octahedral crystal field at each Co atomic site splits the degenerate Co-3*d* band into e_g and t_{2g} sub-bands. The Co-t_{2g} band is lower in energy and is completely filled with six electrons, while the Co-e_g band has one electron per Co atom. Since the narrow Co-e_g band crosses the Fermi surface, any electronic properties of the material are being dominated by the structure of the Co-e_g band and correlations of the electrons in this band. The electronic properties of doped Co chalcogenides, CoS_2 and $CoSe_2$, are directly tied to the degree of interaction between the Co-e_g orbitals and the chalcogen's *p* orbitals. The Co-e_g orbitals expand along the axis towards the chalcogen atoms and hybridize with the antibonding p^* orbitals arising from chalcogen pairs (specifically from the S-3*p* or Se-4*p*) [46], increasing the e_g bandwidth [47]. Calculations indicate that although the lattice constant increases by ~5% when increasing Se content in CoS_xSe_{2-x}, the hybridization is stronger between the e_g and p^* states in $CoSe_2$ than in CoS_2 [48,49], therefore the bandwidth increase of Co-e_g sub-band correlates with increase of Se concentration in CoS_xSe_{2-x}. The slightly increased density of states at the Fermi level in $CoSe_2$ compared to CoS_2 results in higher conductivity (by a factor of two) in the former at room temperature [50]. The width of the Co-3*d* band is determined by the degree of hybridization with the anti-bonding dichalcogen p^* band. As the hybridization is stronger in the $CoSe_2$ case, a continuous decrease in Co-3*d* bandwidth is expected with decreasing Se concentration in CoS_xSe_{2-x}. This change in the d-band bandwidth could have an effect on electrocatalytic processes. Density Functional Theory (DFT) calculated ΔG_{Had} values indicate that CoS_2 is expected to bind H slightly too strong (−0.08 eV, exothermic adsorption) whereas $CoSe_2$ is expected to bind H too weakly (0.49 eV, endothermic adsorption) [24]. Considering ΔG_{Had} as the singular activity descriptor, an intuitive strategy for pushing toward zero HER overpotential on non-PGM TMDs is the manipulation of the electronic structure of Co-based pyrite-group TMDs through controlled chalcogen (anion) doping. It is expected that the addition of small amounts of Se to CoS_2, creating a mixed chalcogen TMD, will bring the doped TMD closer to thermoneutral ΔG_{Had}, increasing HER activity. While the HER activities of CoS_2 and $CoSe_2$ have been shown to be competitive, CoS_2 demonstrates a significant degree of instability in terms of both material and activity loss during potential cycling and extended HER electrolysis [11,13,30,40–44]. The low HER overpotential, for a non-PGM catalyst, and observed instability places CoS_2 in a familiar class of electrocatalytic materials that are characterized by an inverse relationship between activity and stability [2,3,10,51,52]. $CoSe_2$, however, is found to exhibit a higher degree of stability at cathodic potentials [53]. In addition to the manipulation of ΔG_{Had}, it may also be possible to obtain a balance between activity and stability through chalcogen doping of CoS_2 and $CoSe_2$ TMDs.

In this study, we use chalcogen (anion) doped CoS_xSe_{2-x} to assess their impact on the balance between HER activity and material stability. Through potentiodynamic polarization and constant potential electrolysis, we assess the HER activity and discuss the observed trends with regards to standard activity descriptors, hydrogen adsorption free energy (ΔG_{Had}). Additionally, we highlight the importance of material properties beyond the singular activity descriptors, specifically bulk resistivity/conductivity. Finally, we assess the compositional dependent operational stability of the pure and chalcogen (anion) doped TMDs through

a combination of electrochemical and ex-situ quantitative measurements, with the goal of identifying an optimal balance between activity and stability.

2. Experimental

2.1. CoS_xSe_{2-x} material synthesis

Single crystals of CoS_xSe_{2-x} with x ranging from 0 to 2 were grown in the eutectic mixtures of alkali metal salts in a stationary temperature gradient [54,55]. The reactants were sealed in quartz ampules under vacuum and placed in a temperature gradient furnace. The hot zone and cold zone temperatures were 650 °C and 580 °C respectively. The growth temperature was chosen according to the phase diagrams of the Co—S and Co—Se systems [56]. The CoS_xSe_{2-x} charged side of the ampule was placed in the hot zone causing the precursor species to slowly migrate to the cold end of the ampule where the chalcogenide crystals nucleate and grow. Growth of crystals continued for about three weeks.

Upon completion, the crystals were extracted from the solidified alkali salts through ultrasonic assisted dissolution of those salts in a mixture of distilled water, alcohol, and acetone. The recovered crystals were subsequently dried in a muffle furnace at 70 °C for several minutes.

Confirmation of the crystal compositions was achieved through microprobe analysis performed on a digital scanning electronic microscope TESCAN Vega II XMU with energy dispersive micro analysis system INCA Energy 450/XT (20 kV). The analysis showed that the chemical composition of the crystals followed the ratio of initially charged species. No impurity elements belonging to the salts (Cs, K, Na, Cl) were found.

Materials for electrochemical testing were prepared by low energy ball milling (200 rpm) with 5 mm, 8 mm, and 10 mm ceramic beads under an Ar atmosphere. Post ball milling SEM and comparative compositions are shown in Figs. S13 and S14. Notably, no change in composition is observed after ball milling.

2.2. Electrochemical measurements

Electrochemical measurements were performed in 0.1 M perchloric acid ($HClO_4$, Suprapur Millipore Sigma) electrolyte using a three-electrode electrochemical cell with a graphite counter electrode and a Ag/AgCl (BASi) reference electrode. The reference electrode was calibrated in H_2 saturated electrolyte and all potentials are referenced to the reversible hydrogen electrode (RHE). Chalcogenide particle thin films supported on glassy carbon (GC) disks (5 mm in diameter, 0.196 cm^2, HTW GMbH) were used as working electrodes. We have chosen this form factor for the catalyst rather than some morphologically engineered nanostructure as it is amenable to the synthesis procedure which produces a homogeneous distribution of mixed chalcogen composition and provides well-defined crystals for the fundamental investigation. The particles were subsequently suspended in 2-propanol (IPA, electronic grade, 99.999%), and then drop cast onto GC disks. The films were dried under a flow of argon to form a uniform layer. Two µl of 0.05 wt% Nafion (LQ-1105 1100 EW, Ion Power) in IPA were pipetted onto the dried film to secure the particles. Prior to loading with catalyst, the GC disks were polished to a mirror finish using progressively finer diamond paste down to 0.05 µm (Buehler). The GC disks were then sonicated in Millipore water to remove contaminants.

Linear sweep voltammetry (LSV), 20 mV s^{-1} scan rate, was used to assess HER activity in H_2 saturated 0.1 M $HClO_4$ with an Autolab PG Stat 302N potentiostat. Rotation (Pine Instruments rotator, AFMSRCE) was used to remove any evolved bubbles, 1600 rpm. All potentials are compensated for the ohmic drop through the electrolyte as measured by impedance.

Roughness factors (RF) for the catalyst thin films were calculated using electrochemical capacitance measured as a function of potential scan rate between 0.20 and 0.30 V vs. RHE: 20, 30, 50, 100, and 150 mV s^{-1}. See Ref. [57] for detailed procedure. For each scan rate, the potential was cycled at least 5 times to ensure the current response was stable. Overpotential dependent HER currents are normalized by both the geometric area of the GC disk and the RF of the catalyst thin film where the RF of the GC disk is considered to be unity. See Figs. S1 and S2 for capacitance data and RF calculation methodology. To enable direct comparison of catalytic materials, the RF of each drop-cast electrode was matched, to the extent that is possible, to ensure evaluation of electrocatalytic activity on samples with similar electrochemically accessible surface areas. Further compensation of differences in catalyst loading and surface area is accounted for by normalization of HER current by capacitively determined RF.

The potentiostatic electrolysis stability tests were conducted at the desired overpotential with hold times ranging from 10 to 30 min. During electrolysis, the catalytic electrode was rotated at 400 rpm to avoid condensation of dissolved selenium [58] or redeposition of Co and to remove any evolved H_2. The HER activities were measured before and after the stability tests and the aged electrolyte was collected for compositional analysis through ICP-OES (Thermo Scientific iCAP 7000 ICP-OES). Large single crystals of CoS_xSe_{2-x} were affixed to tungsten boats with graphite epoxy for post-electrolysis surface roughness measurement through atomic force microscopy (AFM).

Charge-transfer resistance (CTR) measurements were accomplished through electrochemical impedance spectroscopy (EIS) in the three-electrode cell at −0.2 V vs. RHE over a frequency range from 100 kHz to 5 mHz with a sinusoidal amplitude of 10 mV. The Randles equivalent circuit used to extract the CTR from EIS data is shown as an inset in Fig. S6.

2.3. Material characterization

The morphologies and crystal structures of the chalcogenide crystals were imaged with scanning electron microscopy (SEM, Zeiss Supra 50VP) operated at 8 kV.

Surface roughness measurements were carried out by atomic force microscopy (AFM) in tapping mode, using Bruker Multimode 8 with a silicon tip (Budget Sensors Tap300Al-G; f_0 = 300 kHz, k = 40 N/m). Typical results for Se-rich and S-rich cases are shown in Fig. 7. Before potential holding, all samples have a relatively uniform surface roughness of ρ_{RMS} = 0.42 ± 0.09 nm.

XPS measurements were performed with a PHI Veraprobe 5000 instrument equipped with Monochromated AlK alpha source. Analysis was made with X-ray setting of 100 micrometers 25 W e-beam, photoelectrons were collected using hemispherical analyzer. Pass energy was 117 V for surveys. Dual beam neutralization was performed to compensate depletion of photoelectrons from the surfaces.

X-ray diffraction (XRD) spectra were collected using a Rigaku SmartLab diffractomer with a Cu Kα X-ray source operated at 40 kV and 30 mA.

3. Results and discussion

Slow heterogeneous growth of CoS_xSe_{2-x} in alkali salts yields large, compositionally homogeneous crystals. The pyrite-group single chalcogen and chalcogen-doped TMDs are characterized by a homogeneous dispersion of the chalcogen atoms in an ordered distribution among the unit cells [54–56,59–61]. The growth

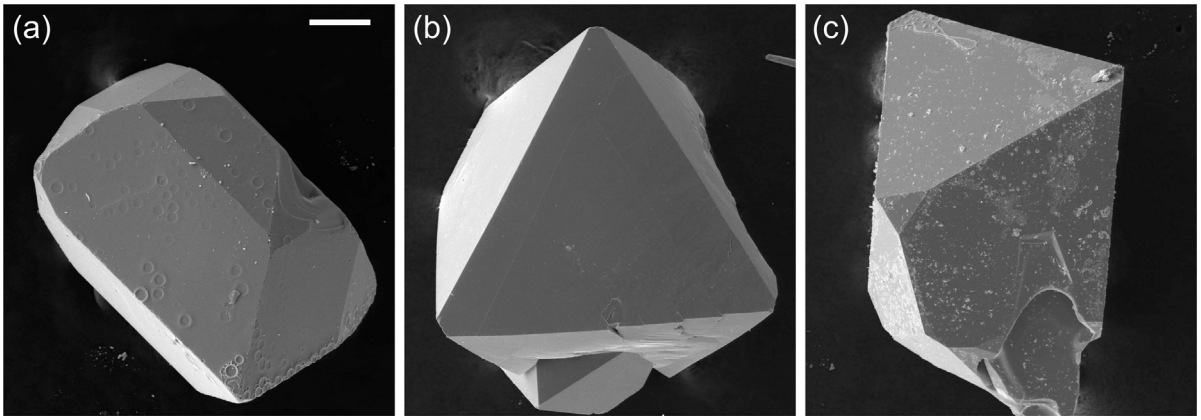

Fig. 1. Scanning electron micrographs (SEM) of representative as-synthesized chalcogenide single crystals: (a) CoS_2, (b) CoS_1Se_1, and (c) $CoSe_2$. Scale bar is 100 μm.

method allows for specific and well-defined control of composition resulting in high purity, ordered crystalline materials, see SEMs in Fig. 1 and S10. In this work we test a range of Co-based pyrite-group TMDs of the general composition CoS_xSe_{2-x} spanning from CoS_2 to $CoSe_2$. XRD spectra for three representative compositions are shown in Fig. 2. These spectra are indicative of the homogeneous, crystalline character of the heterogeneously grown crystals. The lattice parameter of the cubic crystals is found to trend with composition, increasing with decreasing sulfur content (S = 1.78, a = 5.59 Å; S = 0.34, a = 5.82 Å; S = 0.07, a = 5.87 Å). This trend is in line with the lattice parameters for CoS_2 to $CoSe_2$ which are 5.538 Å [11,62] and 5.859 Å [11] respectively.

Polarization curves recorded in H_2 saturated acidic, pH = 1, electrolyte for four representative CoS_xSe_{2-x} compositions are shown in Fig. 3(a). In general agreement with previously published results [11,13,42,44,53,63], CoS_2 and $CoSe_2$ are found to have nearly identical HER activity, in seeming disagreement with DFT calculated ΔG_{Had} values [24]. In contrast, however, to previous studies of mixed chalcogen TMDs [36–39], all intermediate compositions of CoS_xSe_{2-x} tested here exhibit a decreased HER activity, lower current density at a given overpotential (Fig. 3(b)), than pure CoS_2 and $CoSe_2$. Anion doping or partial substitution of chalcogen atoms, namely S and Se, has been shown to result in an increased HER activity for both W and Mo based TMDs [36–39]. The substitution of chalcogen atoms was proposed to affect the strain of the TMD lattice, changing the electronic structure and ΔG_{Had}, as well as introducing more defects onto the surface, increasing the active site density [38]. Further characterization of the material tested in Ref. [38], however, shows an uneven distribution of Se in the mixed chalcogen material. Phase separation and variation in exchange capacity for S and Se resulted in the formation of phase separated regions of S-rich and Se-rich dichalcogenides with a high interfacial area in the doped material. The interface between these phases likely creates sites with a distorted electronic structure resulting in more thermoneutral hydrogen adsorption [38]. Chalcogen doping was also observed to partially change the atomic coordination geometry for WSe_2 from the 2H semiconducting toward the 1T metallic phase [38]. In this case, a significant decrease in the charge transfer resistance due to increased conductivity contributes to the improvement in activity [36–38]. In general, for Mo and W based TMDs, anion/chalcogen doping is found to improve HER activity, either through the formation of an interfaced material or due to the partial or complete transition from a semiconducting to a metallic conducting phase, improving charge transfer.

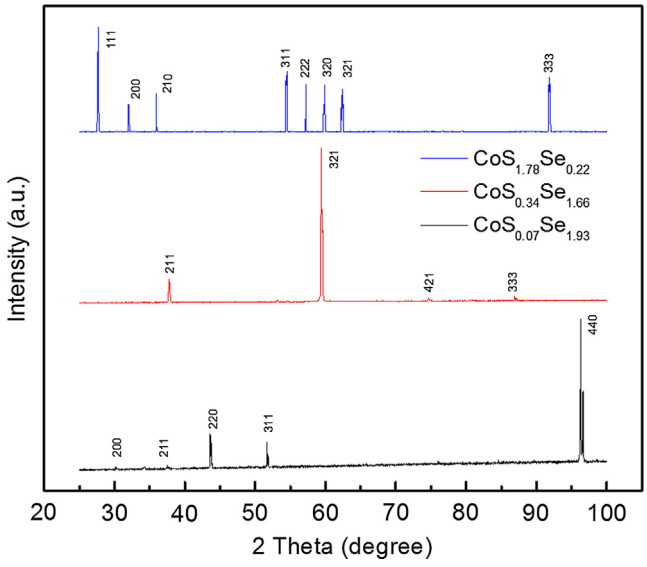

Fig. 2. XRD spectra of representative as-synthesized chalcogenide single crystals: $CoS_{1.78}Se_{0.22}$ (blue), $CoS_{0.35}Se_{1.65}$ (red), and $CoS_{0.08}Se_{1.92}$ (black).

In Fig. 3(b) we have plotted the HER current density, normalized by both the geometric area of the electrode and the relative roughness factor (RF) with respect to the supporting GC electrode, at η = 300 mV as a function of composition. In all cases, the partial chalcogen substitution results in a decrease in HER current density, with the lowest activities being represented by the mid-range compositions. This is in direct contrast to previous reports of anion doped TMDs [36–39] where all combinations of chalcogen substituted TMD compositions resulted in a material with superior HER activity. To begin to develop an understanding of the observed HER activity trend for the chalcogen substituted Co-based pyrite-group TMDs studied here, we determine the Tafel slopes as a function of Se content and overlay the results with the constant overpotential HER current density data, Fig. 3(b). It is expected that the partial substitution of the chalcogen atom will introduce disorder, straining the lattice, shifting the electronic band structure, and increasing the defect and dangling bond density on the surface [36–39], all of which should result in improvements in HER performance. With increasing degree of chalcogen substitution, moving from both the S-rich and Se-rich compositions, the Tafel slope is found to increase, Fig. 3(b), appearing strongly correlated to the observed trend in HER current density at fixed overpotential. Kinetic and microkinetic models of the HER [64–66] offer generalized interpretations of the rate-determining step based on the observed low overpotential Tafel slope. The elementary steps of the HER at acidic pH, hydronium ion reduction, are as follows [65–67]:

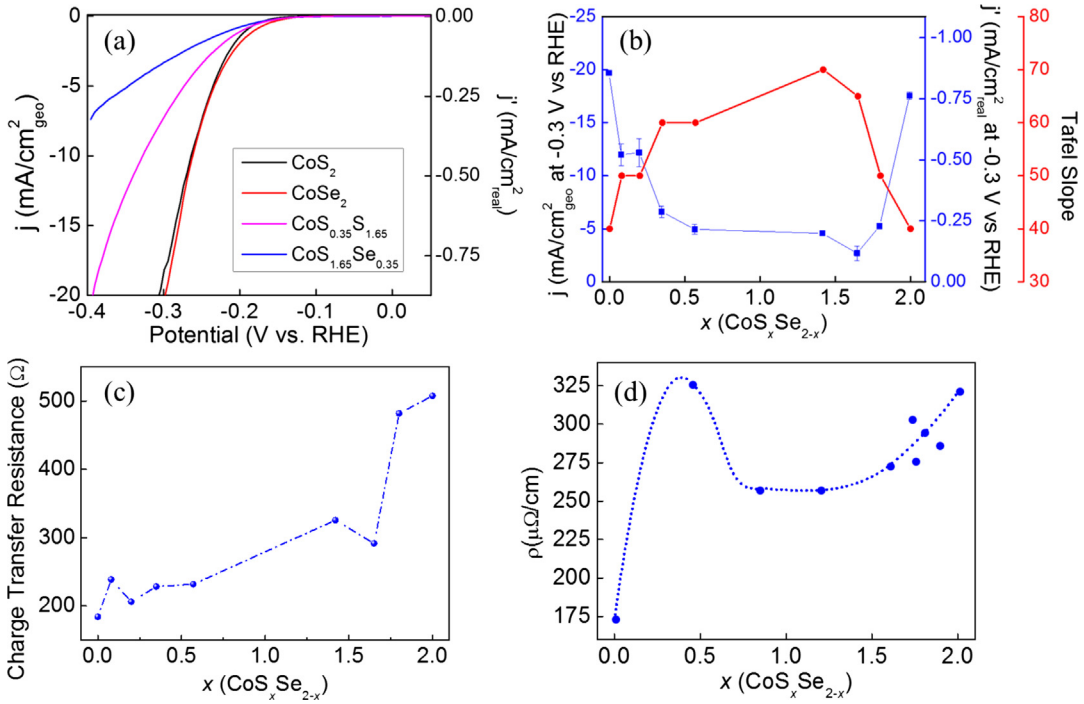

Fig. 3. (a) HER polarization curves in H_2 saturated 0.1 M $HClO_4$, 20 mV s^{-1}, for CoS_2 (black), $CoS_{1.65}Se_{0.35}$ (blue), $CoS_{0.35}Se_{1.65}$ (pink), and $CoSe_2$ (red). In order to make direct comparisons, capacitive RF measurements are used to ensure each electrode has the same electrochemically accessible surface area. Current on left axis is normalized by the geometric area of the electrode; current on the right axis is normalized by the real electrochemically active area (ECSA) as determined by capacitive measurements. (b) HER current density, recorded from HER polarization curves in H_2 saturated 0.1 M $HClO_4$ at 20 mV s^{-1}, at η = 300 mV for CoS_xSe_{2-x} as a function of composition. Current density on the left axis is normalized by the geometric area of the electrode while the current density on the right axis is normalized by the ECSA. A secondary right y-axis presents the Tafel slope, red circles, as a function of composition. (c) Charge transfer resistance (CTR) for the HER as a function of CoS_xSe_{2-x} composition. (d) Bulk resistivity of CoS_xSe_{2-x} as a function of composition at 300 K. The dashed line is a guide to the eye. Adapted from Ref. [50].

$$\text{Volmer Step:} \quad H_3O^+ + e^- + M \rightleftharpoons M - H + H_2O \tag{1}$$

$$\text{Heyrovsky Step:} \quad M - H + H_3O^+ + e^- \rightleftharpoons H_2 + H_2O + M \tag{2}$$

$$\text{Tafel Step:} \quad 2M - H \rightleftharpoons H_2 + 2M \tag{3}$$

Low overpotential Tafel slopes of 116, 39, or 29 mV dec^{-1} are indicative of a Volmer, Heyrovsky, or Tafel reaction rate-determining step respectively [64–67]. Fitting of the Tafel slope to experimental data, especially for nanoscale materials that are far from model systems, is relatively ambiguous as often multiple slopes can be fit to the data due to the potential dependence of the hydrogen coverage [65,66]. With that said, we can gain a cursory understanding of any mechanistic shifts by assessing the change in low overpotential Tafel slope with CoS_xSe_{2-x} composition. The trend in Fig. 3(b) indicates a shift away from the theoretically expected values of the Tafel slope derived from the kinetics of the elementary steps for the intermediate compositions of the doped TMDs. Deviation from the expected Tafel slopes can be attributed to: (1) intermediate hydrogen coverage, θ_H, (2) potential dependent hydrogen coverage at HER relevant potentials, and/or (3) a significant activation barrier for the Volmer step [64–67]. The Volmer step barrier can be related to the adsorption free energy of hydrogen which, if too high, M-H_{ad} will not form, or the resistivity of the material which can limit the rate of charge transfer to the M-H_{ad} intermediate.

Electrochemical impedance spectroscopy (EIS) can be used to quantify the charge transfer resistance (CTR) for the HER (see Fig. S6 for Nyquist plots). The HER CTR for CoS_xSe_{2-x} is plotted in Fig. 3(c). CTR is a measure of the ease with which H_{ad} forms on the surface and is controlled by both the free energy of adsorption for H_{ad} ($\Delta G_{H_{ad}}$) and the electrical conductivity of the catalytic material. CTR values are extracted from the Nyquist plots in Fig. S6 using the equivalent circuit in the figure inset. A continuous decrease in the CTR is observed with increasing Se content where $CoSe_2$ is found to have the lowest CTR. The CTR trend observed in Fig. 3(c) as a function of anion doped TMD composition does not necessarily fit the one expected from the constant overpotential current density and Tafel slope trends shown in Fig. 3(b). However, if we consider the compositional dependence of the bulk resistivity, which is often overlooked for pyrite-structured Co-based TMDs due to their intrinsic metallic behavior, we can gain some insight into both the activity (Fig. 3(b)) and CTR (Fig. 3(c)) trends. Namely, the compositional determined activity trend observed in Fig. 3(b) is a consequence of a convolution of hydrogen adsorption free energy and material conductivity. A quick note: even though the Co-based pyrite-group TMDs, as well as some other bulk and two-dimensional TMDs, exhibit metallic electronic behavior [5,7,11,13,17,36,38,40,41], their resistivity is still two orders of magnitude higher than that for traditional metallic electrocatalysts such as Pt [50,68]. The higher resistivity for metallic TMDs, in comparison to Pt, is manifested as a greater proportional impact of the resistivity as a function of composition. As observed in Fig. 3(d), resistivity is a relatively weak function of composition, with an anomalous point at $x \sim 1.5$, until approaching $CoSe_2$ where a precipitous decrease leaves $CoSe_2$ with a resistivity nearly half that of the other compositions. Generally, the trend in CTR with composition correlates well to that of measured resistivity.

Moving from CoS_2 to $CoSe_2$ transitions from a surface that binds hydrogen slightly too strong, $\Delta G_{H_{ad}} = -0.08$ eV for CoS_2, to one that binds hydrogen too weak, $\Delta G_{H_{ad}} = 0.49$ eV for $CoSe_2$ [24]. This trend is considering a hydrogen adsorbing on a terminal S/Se atom coordinated to a transition metal atom [24]. It is expected then that as we sequentially substitute S with Se, moving toward $CoSe_2$, the

average ΔG_{Had} of the surface should first pass through a thermoneutral value, $\Delta G_{Had} = 0$, before moving to the more endothermic adsorption free energy of $CoSe_2$. This compositional dependent ΔG_{Had} would then be expected to result in a peak in activity for the anion doped Co TMDs; this is not what we observe, Fig. 3(b). At this point, there is limited DFT analysis of mixed chalcogen TMDs due to the complexity of the electronic interactions between the three constitutive species and the variability of surface structure, defect density, and composition. However, one such effort calculated a decrease in the hydrogen adsorption free energy, more thermoneutral, when MoS_2 is doped with Se. For Mo and W based TMDs (MX_2 where M = Mo, W and X = S, Se), however, anion doping results in a transition from a semiconducting to metallic material [5,8,9,12,15,17,18,36–40]. This change in electronic character is dominant over any change in the free energy of adsorption of hydrogen with composition, resulting in the overall increase in activity beyond the single chalcogen TMDs. For Co-based pyrite-group TMDs, in contrast, all compositions have metallic character and the resistivity is a much weaker function of composition, Fig. 3(d). The purported motivation for anion doping of Co-based pyrite-group TMDs is to bring the ΔG_{Had} closer to the optimal thermoneutral value. This is assuming that the effect of doping CoS_2 with Se, for example, would essentially be a compositional dependent weighted average of the ΔG_{Had} of the two single chalcogen TMDs. However, any deviation from the pure compositions is found to result in a decrease in activity. This suggests that our initial assumption was too simplistic. The ΔG_{Had} on the surface of the TMDs that evolves due to anion doping is likely a convolution of charge redistribution, orbital hybridization, and geometric changes to the material lattice that combine to define the adsorptive properties of the surface. We purport that the intrinsic activity of the surface is defined by the convolution of ΔG_{Had} and the material electrical conductivity (resistivity). As the composition approaches $CoSe_2$, the activity again begins to increase (Fig. 3(b)), approaching that of CoS_2, as the low resistivity compensates for the relatively high endothermicity of hydrogen adsorption on $CoSe_2$ (0.49 eV [24]) in comparison to the small exothermic deviation of CoS_2 from thermoneutral ΔG_{Had} (−0.08 eV [24]). As we approach high Se content compositions, the resistivity becomes strongly dependent on Se concentration, dropping significantly (increasing conductivity) approaching $CoSe_2$ (Fig. 3(d)). These results highlight the potential error inherent in using ΔG_{Had} as the sole activity descriptor for non-PGM TMDs.

Concern for the corrosion resistance and stability of HER electrocatalytic materials, even those composed of non-PGM materials, is often understated due to the reductive cathodic operating potentials for the HER, <0 V vs. RHE. At these reductive potentials, materials are often assumed to be intrinsically stable. An unwritten adage in electrocatalysis, one that is supported by numerous experimental studies [2,10,51,52,69], frames the activity-stability relationship as one of inverse proportionality. Active catalysts are not stable and stable catalysts are not active. The challenge for catalyst development then becomes to find the proper balance between activity and stability that affords adequate performance and longevity for commercial applicability.

While CoS_2 exhibits higher HER current densities at a given overpotential than any of the doped chalcogen TMD compositions, we observe a quick decay upon constant potential electrolysis, Fig. 4 and Fig. S8. After 30 min at −300 mV vs. RHE, the catalytic HER activity has decayed to nearly zero. This high rate of decay in activity was also observed for other first-row MS_2 TMDs [11]. The rate of activity decay is found to be potential dependent, where faster rates, measured as a percent decrease in HER polarization current at any given overpotential for a fixed electrolysis time, are observed at larger overpotentials, Fig. 4(b). This cathodic potential dependent activity decay suggests that catalyst deactivation may be initiated by the formation of a surface passivating reduced species rather than some traditional corrosion process. Analysis of the post-electrolysis Co and S 2p XPS spectra, Fig. 5, S3, S4, and Table S1, support this conclusion. The pre-electrolysis S 2p XPS spectra for CoS_2 consists of a S $2p_{1/2}$ and $2p_{3/2}$ doublet with major peaks at 162.4 and 161.3 eV, respectively. The location and intensity of these peaks are in agreement with previous XPS results for CoS_2 and other pyrite structured TMDs [44,70–75]. It is possible that more than one $2p_{1/2}/2p_{3/2}$ doublet exists, indicating the existence of more than one chemical state. This has been observed previously for other pyrite-group TMDs when well-defined S standards aid the deconvolution of the peaks to identify the different chemical/oxidation states of S [20,28,31,32,70–73,76]. The location of the peaks in Figs. 5 and S4 suggest a general −2 oxidation state for the S in the as-made CoS_2 [19–21,28,31,39,72,74,76–78]. There is a general consensus that the lower energy peak ($2p_{3/2}$) or lower energy doublets centered around 161 eV, are associated with terminal S_2^{2-}/S^{2-} while the higher energy peak ($2p_{1/2}$) and doublets, centered around 162 eV, are associated with bridging S_2^{2-} and apical S^{2-} which is more typical of bulk S [19,28,39,76,79]. After extended electrolysis, a general shift to higher energy is observed for all peaks with a redistribution of intensity from the $2p_{3/2}$ peak to the $2p_{1/2}$ peak which is indicative of a decrease in terminal, anionic S groups. We also observe the appearance of a peak

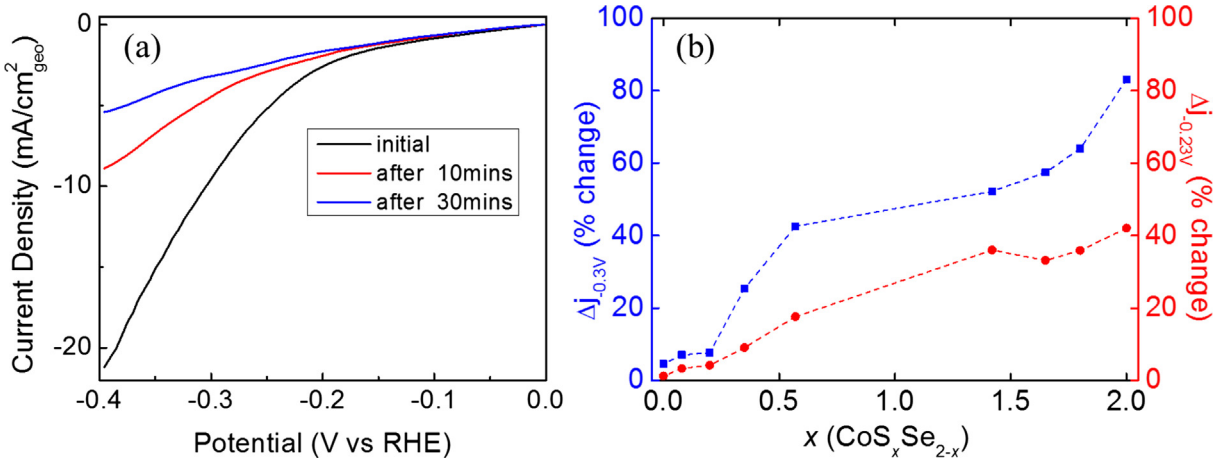

Fig. 4. (a) HER polarization curves for CoS_2 in H_2 saturated 0.1 M $HClO_4$, 20 mV s^{-1}, after 0 (black), 10 (red), and 30 (blue) minutes of constant potential electrolysis at −0.3 V vs. RHE. (b) Percent change in HER current density, extracted from pre- and post-electrolysis potentiodynamic HER polarization curves at −0.3 V vs. RHE in H_2 saturated 0.1 M $HClO_4$ at 20 mV s^{-1}, after 30 min constant potential electrolysis in H_2 saturated 0.1 M $HClO_4$ at −0.3 (blue) and −0.23 (red) V vs. RHE.

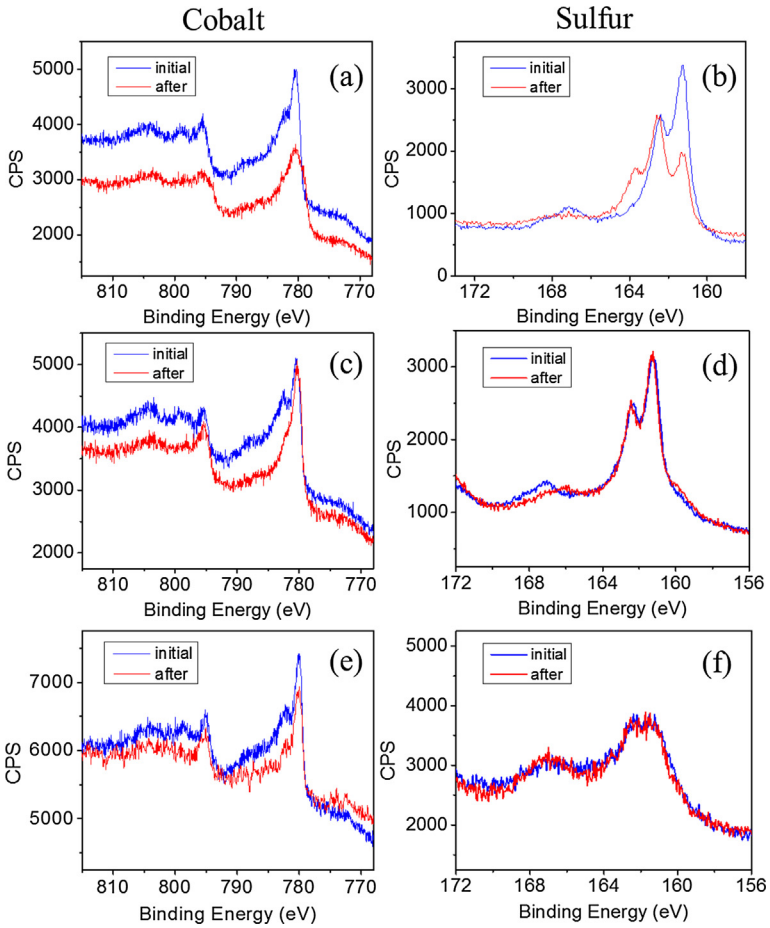

Fig. 5. XPS spectra of the Co 2p (a), (c), (e) and S 2p (b), (d), (f) contribution for CoS_2 (a) and (b), $CoS_{1.8}Se_{0.2}$ (c) and (d), and $CoS_{0.57}Se_{1.43}$ (e) and (f), before (blue) and (after) constant potential electrolysis at −0.3 V vs. RHE for 30 min.

between 164 and 165 eV which can be related to the presence of some more reduced polysulfide species, S_n^{2-} ($2 < n < 8$) [71,74,75]. The peak at ~167 eV has been assigned to sulfate species due to the presence of oxygen [74]. There is also likely a contribution from Se $3p_{1/2}$, as it overlaps with the S 2p peaks, in the Se containing samples to the feature at 167 eV [36]. Comparison of the pre- and post-electrolysis Cobalt 2p spectra in Fig. 5(a-c) shows a general decrease in peak intensity after extended electrolysis. Deconvolution of the Co $2p_{3/2}$ peaks, Fig. S3, shows a loss in the higher energy Co^{2+} and Co^{3+} (783–789 eV) [80–82] features and a general decrease in intensity of the Co—S peak at 780 eV [80–82]. This change in XPS signature is indicative of a general decrease in the concentration of higher valent and S-bonded Co in the surface and near surface region of the catalyst after extended electrolysis. Analysis of Co $2p_{1/2}$ peaks, Fig. S3, indicates the presence of Co^{2+} and Co^{3+} species [83], the proportions of which change after extended electrolysis. In both pre- and post-electrolysis spectra, there is an absence of metallic Co which is expected to show a peak at 793 eV [83].

Analysis of the stability of other pyrite-type structures under a range of conditions have shown that it is possible for the metal atom to donate electrons to the coordinating S atoms, forming a more reduced sulfide species and a metal cation [72,75]. This mechanism is potentially operative here as XPS data indicate an enrichment in reduced S, possibly polysulfides, on the surface along with a decrease in the number of Co—S bonds in the near surface region. This reduction in surface Co is matched by a presence of Co in solution as measured through ICP-OES. Compositional analysis from the XPS data indicate a general enriching of S in the catalyst surface/near surface regions after extended electrolysis as well as a general change in the average coordination of the S; shifting from a terminal anion to a bridged S with increased coordination. Computational assessment of the optimal site for hydrogen adsorption on layered TMDs indicate that hydrogen adsorbs on the low coordinated terminal S on the transition metal edge [15,24,25,84]. There is no reason to believe that this insight cannot also be applied to the HER on fractured pyrite-group surfaces. After only 30 min of constant overpotential electrolysis, the HER activity of CoS_2 decays to nearly zero (Fig. 4). While dissolved Co is found in solution, the near complete loss in HER activity does not coincide with complete dissolution of the catalytic material. The XPS results indicate that the activity loss is associated with the formation of a passivating reduced polysulfide film on the surface and a decrease in the presence of Co coordinated terminal anions. As evidenced by the composition dependence of the activity decay (Fig. 4(b)) the substitution of S with even small fractions of Se dramatically improves the stability of the material through retention of a high density of Co-coordinated terminal anions (X_2^{2-} and X^{2-}), Figs. S3 and S4.

Further assessment of the potential and composition dependent degradation of the di-chalcogen TMDs at HER relevant potentials is shown in Figs. 6 and 7. By plotting the change in surface roughness between pre- and post-extended electrolysis, Fig. 6, we observe only small roughness differences for $x < 1.5$, where stability increases with increasing Se content. A more pronounced decrease in stability can be observed at $x \geqslant 1.5$, where the roughness

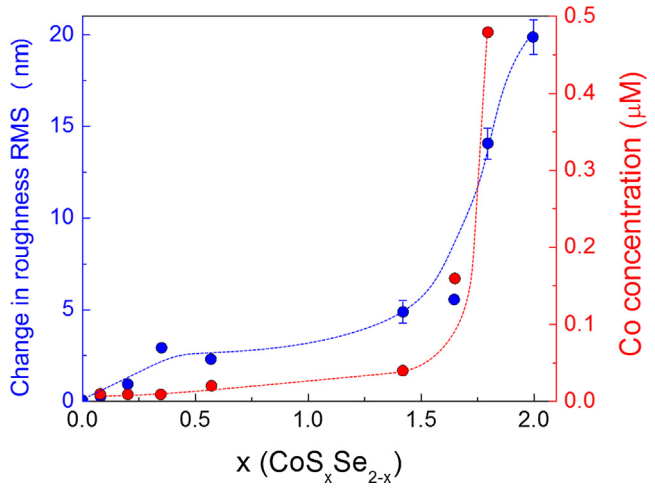

Fig. 6. Compositional dependence (CoS_xSe_{2-x}) of surface morphology evolution and material dissolution. The change in surface roughness, comparing pre- and post-electrolysis (−0.3 V vs. RHE for 30 min. in H_2 saturated 0.1 $MHClO_4$), is depicted in blue and the post electrolysis concentration of Co in the electrolyte is shown in red. Both measurements show a rapid decrease in stability for x > 1.5. Dotted lines are spline fits meant as a guide for the eye.

increases dramatically and the morphology of the surface changes, acquiring a granular texture (Fig. 7). The evolution in surface roughness correlates well with ICP-OES measurements. An inverse activity-stability relationship can be observed for the compositional progression from CoS_2 to Se-rich CoS_xSe_{2-x}, Fig. 3(b), excluding $CoSe_2$. Analysis of the 238 nm Co emission line of the ICP-OES spectra is presented as the red curve in Fig. 6. The trend follows that of the AFM roughness measurements: At x < 1.5, the Co concentration is at or barely above baseline with only moderate dependence on anion doping. At $x \geqslant 1.5$, the rapid increase of the Co concentration in the electrolyte as well as the increase in the roughness of the surface indicates significant morphological and compositional instability of the catalyst during HER. The observed compositional trend in stability agrees with conclusions derived from DFT calculations for 2-dimensional MoS_2 and transition metal doped MoS_2 where the negative linear scaling between the adsorption energy of the chalcogen atoms coordinating the metal and hydrogen on the active chalcogen atoms indicates that a stronger interaction between H and X will be matched by a weaker interaction between X and M (where X is the chalcogen and M is the transition metal species in the TMD) [15]. Here we find that CoS_2 is the least stable while $CoSe_2$ is the most stable. This is in accord with their calculated hydrogen adsorption free energies: ΔG_{Had} (CoS_2) = −0.08 eV, ΔG_{Had} ($CoSe_2$) = 0.49 eV [24]. The stronger H—S bond in CoS_2 compared to the H—Se bond in $CoSe_2$, according to the inverse linear scaling calculated in Ref. [15], indicates that the Co—S bond is expected to be weaker than the Co—Se bond. All of our qualitative and quantitative corrosion/stability assessment methodologies demonstrate this relationship to be valid with $CoSe_2$ exhibiting the highest degree of stability among

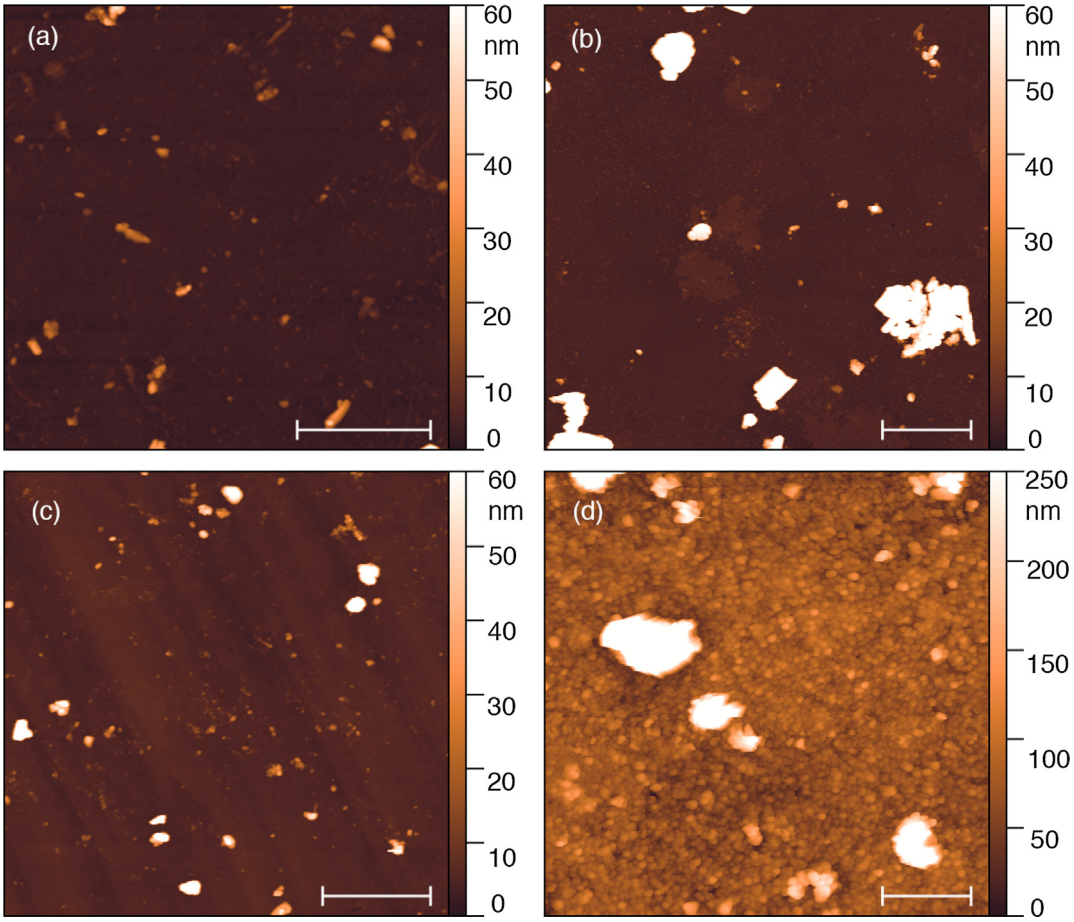

Fig. 7. AFM topography images before (left column) and after (right column) extended electrolysis at −0.3 V vs. RHE in H_2 saturated 0.1 $MHClO_4$. Top row shows surface of a Se-rich (x = 0.08) crystal, with minimal changes before and after HER (a and b, respectively). Bottom row shows a S-rich sample (x = 0.8), where the surface before electrolysis (c) looks qualitatively similar to the previous case (a), but the roughness and morphology of the surface change after electrolysis is significantly different (d). Scale bars are 1 μm.

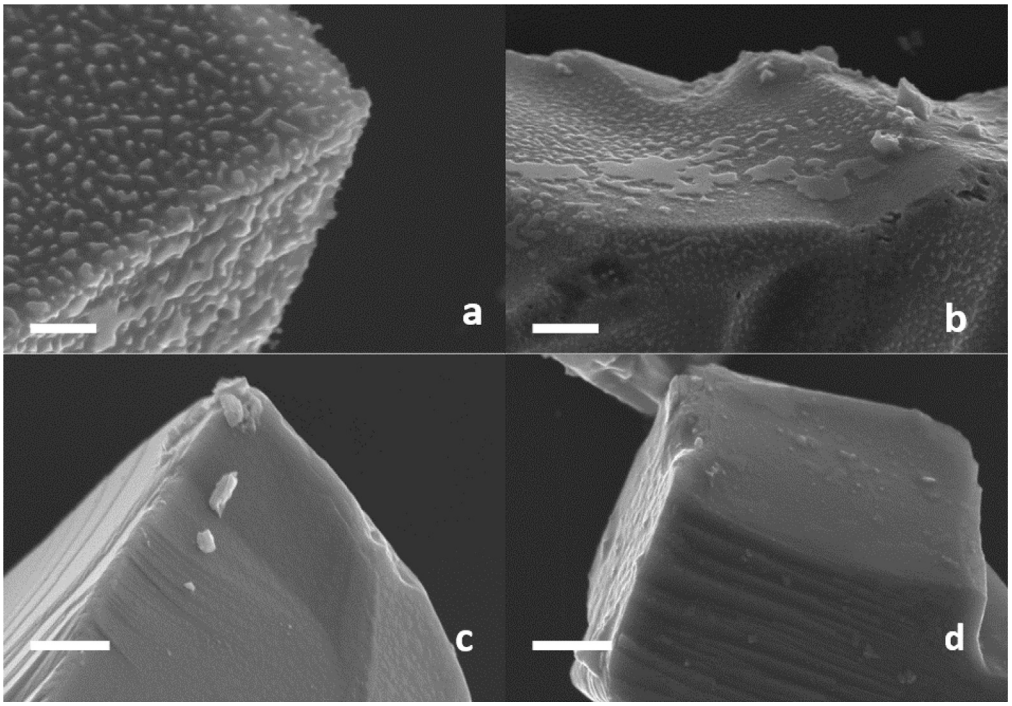

Fig. 8. SEMs of CoS_xSe_{2-x} TMDs after constant potential electrolysis at −0.3 V vs. RHE for 30 min in H_2 saturated 0.1 M$HClO_4$ at room temperature. $CoS_{1.65}Se_{0.35}$ (a), $CoS_{1.42}Se_{0.58}$ (b), $CoS_{0.35}Se_{1.65}$ (c), $CoS_{0.20}Se_{1.80}$ (d). Scale bar is 200 nm.

the range of compositions tested. As our catalysts were initially in the form of well-defined bulk crystals prior to ball milling, we are able to observe the macro-scale corrosion that occurs during constant potential electrolysis as a function of potential. Figs. 8, S11, and S12 contain SEMs of pure CoS_2 and $CoSe_2$ as well as S-rich and Se-rich crystals after extended electrolysis. Dramatic changes in surface morphology after short constant potential electrolysis (30 min) are observed for the sulfur-rich Co-based pyrite-group crystals, while minimal change in surface morphology and roughness is found for the Se-rich crystals. Additionally, for the S-rich crystals, a qualitative potential dependence of the rate and degree of degradation is observed in Fig. S11. At higher overpotentials, comparing Figs. S11(c) to S11(d), a greater degree of surface roughness is observed. This potential dependence lends support to the reductive formation of soluble polysulfides as the material and activity degradation mechanism. This result agrees with the other metrics for assessing and quantifying the compositional dependent stability including ICP-OES (Figs. 4(b), 5, 6, S3, and S4).

The link between activity and stability is often overlooked in the pursuit of higher activities. Nowhere is this more true than in the development of HER electrocatalysts with a goal of replacing Pt-based materials. At potentials below 0 V vs. RHE, a false sense of security is perpetuated and all materials are superficially considered to be stable at these reducing conditions. It is true that anodic dissolution is of no concern at HER relevant potentials for PGM and non-PGM materials alike. However, catalyst deactivation due to surface passivation, reductive dissolution through the formation of a water soluble species causing a change in surface composition, and cathodic corrosion all affect the performance stability of these catalytic materials. As exemplified for other electrocatalytically driven reactions, activity and stability are inversely related [2,10,51,52,69]. It is encouraging, then, that we observe a departure from this inverse relationship for $CoSe_2$ in the series of pyrite-group TMDs studied here. The combination of ΔG_{Had}, resistivity, and reductive stability for the Co-based TMDs and mixed chalcogen TMDs highlights the importance of moving beyond single activity descriptors and presents $CoSe_2$ as an active and stable non-PGM electrocatalyst that breaks away from the typical activity-stability scaling. Further development of HER electrocatalysts based on $CoSe_2$ should focus on optimization of the nanoscale structure to increase active site exposure and geometric density.

4. Conclusions

Here we have presented a careful and through assessment of the compositional dependent HER activity and stability for Co-based mixed chalcogen, CoS_xSe_{2-x}, pyrite-group TMDs. In direct contrast to other reports on mixed chalcogen TMDs that have been limited to Mo and W [36–39], we observe a decrease in HER activity for any departure from the pure, single chalcogen TMD compositions, CoS_2 and $CoSe_2$. For Mo and W, the improvement in activity with the incorporation of a second chalcogen atom to the lattice is likely related to the shift from semiconducting to metallic electronic behavior, which dominates any change in ΔG_{Had}. For Co-based pyrite-group TMDs, all compositions are found to have metallic character, and the addition of a second chalcogen atom does not change this fact. We conclude that the observed compositional trend in HER activity is due to the combination of compositional dependent ΔG_{Had} and bulk resistivity/conductivity of the pyrite-group TMDs. While CoS_2 is found to have near thermoneutral hydrogen adsorption free energy, it has the highest resistivity among the compositions tested. The decrease in HER activity with anion doping is proposed to be related to both the de-optimization of ΔG_{Had} and weak dependence of resistivity on composition for a large fraction of the anion doped compositional space between CoS_2 and $CoSe_2$. As the composition approaches $CoSe_2$, however, the HER activity is regained even with endothermic H-adsorption [24]. Bulk resistivity of the pure and mixed chalcogen TMDs as well as the charge transfer resistance for the HER is found to be most optimal for $CoSe_2$, with a linear improvement with composition moving away from CoS_2. This highlights the convolution of hydrogen adsorption free energy and material conductivity in determining the HER activity for even TMDs that display metallic electronic

character. In addition, $CoSe_2$ exhibits the highest degree of stability under constant potential HER electrolysis. Sulfur-rich Co-based pyrite-group TMDs are found to quickly deactivate through loss of Co and formation of a passivating reduced S species at the surface. With an HER activity matching that of CoS_2, but with a dramatic improvement in stability, $CoSe_2$ breaks away from the traditional inverse activity – stability relationship and represents a promising material for non-PGM HER electrocatalysis in acidic PEM electrolyzers. Future work related to the engineering and design of nanoscale morphology for $CoSe_2$ could lead to the development of a next-generation, non-PGM HER electrocatalyst with an optimal activity – stability balance.

Acknowledgements

We would like to acknowledge financial support by the CRDF Global grant OISE-16-62115-0 and FSCX-16-62112-0. The work at Drexel University was partially supported by DARE-BRAVE Grant, as part of the Drexel's Areas of Research Excellence Initiative, and the National Science Foundation through the Catalysis Program in the Division of Chemical, Biological, Environmental and Transport Systems, under Award No. 1602886. Part of the work was supported by the Center for the Computational Design of Functional Layered Materials (CCDM), an Energy Frontier Research Center funded by the U.S. Department of Energy, Office of Science, Basic Energy Sciences under Award # DE-SC0012575. We gratefully acknowledge Dmitri Barbash in the Core Facilities in the College of Engineering at Drexel University for help with XPS measurements.

Appendix A. Supplementary material

Supplementary data associated with this article can be found, in the online version, at https://doi.org/10.1016/j.jcat.2018.07.030.

References

[1] Hydrogen Storage: Fuel Cell Technologies Office, 2016.
[2] Nemanja Danilovic, Ramachandran Subbaraman, Kee Chul Chang, Seo Hyoung Chang, Yijin J. Kang, Joshua Snyder, Arvydas P. Paulikas, Dusan Strmcnik, Yong Tae Kim, Deborah Myers, Vojislav R. Stamenkovic, Nenad M. Markovic, Activity-stability trends for the oxygen evolution reaction on monometallic oxides in acidic environments, J. Phys. Chem. Lett. 5 (14) (2014) 2474–2478.
[3] Nemanja Danilovic, Ramachandran Subbaraman, Kee Chul Chang, Seo Hyoung Chang, Yijin Kang, Joshua Snyder, Arvydas Paul Paulikas, Dusan Strmcnik, Yong Tae Kim, Deborah Myers, Vojislav R. Stamenkovic, Nenad M. Markovic, Using surface segregation to design stable Ru-Ir oxides for the oxygen evolution reaction in acidic environments, Angew. Chem. – Int. Ed. 53 (51) (2014) 14016–14021.
[4] Serhiy Cherevko, Simon Geiger, Olga Kasian, Andrea Mingers, Karl J.J. Mayrhofer, Oxygen evolution activity and stability of iridium in acidic media. Part 1. – Metallic iridium, J. Electroanal. Chem. 773 (2016) 69–78.
[5] Damien Voiry, Maryam Salehi, Rafael Silva, Takeshi Fujita, Mingwei Chen, Tewodros Asefa, Vivek B. Shenoy, Goki Eda, Manish Chhowalla, Conducting MoS nanosheets as catalysts for hydrogen evolution reaction, Nano Lett. 13 (12) (2013) 6222–6227.
[6] Desheng Kong, Haotian Wang, Judy J. Cha, Mauro Pasta, Kristie J. Koski, Jie Yao, Yi Cui, Synthesis of MoS_2 and $MoSe_2$ films with vertically aligned layers, Nano Lett. 13 (3) (2013) 1341–1347.
[7] M. Chhowalla, H. Shin, G. Eda, L. Li, K. Loh, H. Zhang, The chemistry of two-dimensional layered transition metal dichalcogenide nanosheets, Nat. Chem. 5 (2013) 263–275.
[8] S. Siahrostami, C. Tsai, M. Karamad, R. Koitz, M. Garcia-Melchor, M. Bajdich, A. Vojvodic, Norskov J. Abild-Pedersen, F. Studt, Two-dimensional materials as catalysts for energy conversion, Catal. Lett. 146 (10) (2016) 1917–1921.
[9] Jesse D. Benck, Thomas R. Hellstern, Jakob Kibsgaard, Pongkarn Chakthranont, Thomas F. Jaramillo, Catalyzing the hydrogen evolution reaction (HER) with molybdenum sulfide nanomaterials, ACS Catal. 4 (11) (2014) 3957–3971.
[10] Jakub Staszak-Jirkovský, Christos D.D. Malliakas, Pietro P.P. Lopes, Nemanja Danilovic, Subrahmanyam S.S. Kota, Kee-Chul Chang, Bostjan Genorio, Dusan Strmcnik, Vojislav R.R. Stamenkovic, Mercouri G. Kanatzidis, Nenad M. Markovic, Design of active and stable Co-Mo-S_x chalcogels as pH-universal catalysts for the hydrogen evolution reaction, Nat. Mater. 15 (2016) 197–204.
[11] Desheng Kong, Judy J Cha, Haotian Wang, Hye Ryoung Lee, Yi Cui, First-row transition metal dichalcogenide catalysts for hydrogen evolution reaction, Energy Environ. Sci. 6 (12) (2013) 3553.
[12] Thomas F. Jaramillo, Kristina P. Jørgensen, Jacob Bonde, Jane H. Nielsen, Sebastian Horch, Ib Chorkendorff, Identification of active edge sites for electrochemical H_2 evolution from MoS_2 nanocatalysts, Science (New York, N.Y.) 317 (July) (2007) 100–102.
[13] Matthew S. Faber, Mark a. Lukowski, Qi Ding, Nicholas S. Kaiser, Song Jin, Earth-abundant metal pyrites (FeS_2, CoS_2, NiS_2, and their alloys) for highly efficient hydrogen evolution and polysulfide reduction electrocatalysis, J. Phys. Chem. C 118 (2014) 21347–21356.
[14] Berit Hinnemann, Poul Georg Moses, Jacob Bonde, Kristina P. Jorgensen, Jane H. Nielsen, Sebastian Horch, Ib Chorkendorff, Jens K. Nørskov, Biomimetic hydrogen evolution: MoS_2 nanoparticles as catalyst for hydrogen evolution, J. Am. Chem. Soc. 127 (15) (2005) 5308–5309.
[15] Charlie Tsai, Karen Chan, Jens K. Nørskov, Frank Abild-pedersen, Understanding the reactivity of layered tranistion-metal sulfides: a single electronic descriptor for structrue and adsorption, J. Phys. Chem. Lett. 5 (2014) 3884–3889.
[16] Yongfu Sun, Shan Gao, Fengcai Lei, Yi Xie, Atomically-thin two-dimensional sheets for understanding active sites in catalysis, Chem. Soc. Rev. 44 (3) (2015) 623–636.
[17] Mark A. Lukowski, Andrew S. Daniel, Fei Meng, Audrey Forticaux, Linsen Li, Song Jin, Enhanced hydrogen evolution catalysis from chemically exfoliated metallic MoS_2 nanosheets, J. Am. Chem. Soc. 135 (28) (2013) 10274–10277.
[18] H. Wang, Z. Lu, S. Xu, D. Kong, J. Cha, G. Zheng, P. Hsu, K. Yan, D. Bradshaw, F. Prinz, Y. Cui, Electrochemical tuning of vertically aligned MoS_2 nanofilms and its application in improving hydrogen evolution reaction, PNAS 110 (49) (2013) 19701–19706.
[19] Jue Hu, Bolong Huang, Chengxu Zhang, Zilong Wang, Yiming An, Dan Zhou, He Lin, Michael K.H. Leung, Shihe Yang, Engineering stepped edge surface structures of MoS_2 sheet stacks to accelerate the hydrogen evolution reaction, Energy Environ. Sci. 10 (2017) 593–603.
[20] Haotian Wang, Charlie Tsai, Desheng Kong, Karen Chan, Frank Abild-Pedersen, Jens K. Nørskov, Y. Cui, Transition-metal doped edge sites in vertically aligned MoS2 catalysts for enhanced hydrogen evolution, Nano Res. 8 (2) (2015) 566–575.
[21] Jakob Kibsgaard, Zhebo Chen, Benjamin N. Reinecke, Thomas F. Jaramillo, Engineering the surface structure of MoS_2 to preferentially expose active edge sites for electrocatalysis, Nat. Mater. 11 (11) (2012) 963–969.
[22] Berit Hinnemann, Poul Georg Moses, Jens K. Nørskov, Chemistry of one-dimensional metallic edge states in MoS_2 nanoclusters, Nanotechnology 14 (2003) 385–389.
[23] Sang Chul Lee, Jesse D. Benck, Charlie Tsai, Joonsuk Park, Ai Leen Koh, Frank Abild-Pedersen, Thomas F. Jaramillo, Robert Sinclair, Chemical and phase evolution of amorphous molybdenum sulfide catalysts for electrochemical hydrogen production, ACS Nano 10 (1) (2016) 624–632.
[24] Jinsong Wang, Jia Liu, Bao Zhang, Xiao Ji, Kui Xu, Chi Chen, Ling Miao, Jianjun Jiang, The mechanism of hydrogen adsorption on transition metal dichalcogenides as hydrogen evolution reaction catalyst, Phys. Chem. Chem. Phys. 19 (2017) 10125–10132.
[25] Charlie Tsai, Karen Chan, Jens K. Nørskov, Frank Abild-Pedersen, Rational design of MoS_2 catalysts: tuning the structure and activity via transition metal doping, Catal. Sci. Technol. 5 (1) (2015) 246–253.
[26] Jesse D. Benck, Zhebo Chen, Leah Y. Kuritzky, Arnold J. Forman, Thomas F. Jaramillo, Amorphous molybdenum sulfide catalysts for electrochemical hydrogen production: Insights into the origin of their catalytic activity, ACS Catal. 2 (9) (2012) 1916–1923.
[27] Mohnish Pandey, Aleksandra Vojvodic, Kristian S. Thygesen, Karsten W. Jacobsen, Two-dimensional metal dichalcogenides and oxides for hydrogen evolution: a computational screening approach, J. Phys. Chem. Lett. 6 (9) (2015) 1527–1585.
[28] Yilin Deng, Louisa Rui Lin Ting, Perlin Hui Lin Neo, Yin-Jia Zhang, Andrew A. Peterson, Boon Siang Yeo, Operando Raman spectroscopy of amorphous molybdenum sulfide (MoS_x) during the electrochemical hydrogen evolution reaction: identification of sulfur atoms as catalytically active sites for H^+ reduction, ACS Catal. 6 (2016) 7790–7798.
[29] M.V. Bollinger, J.V. Lauritsen, K.W. Jacobsen, J.K. Nørskov, S. Helveg, F. Besenbacher, One-dimensional metallic edge states in MoS_2, Phys. Rev. Lett. 87 (19) (2001) 196803.
[30] Chuan Xia, Hanfeng Liang, Jiajie Zhu, Udo Schwingenschlögl, Husam N. Alshareef, Active edge sites engineering in nickel cobalt selenide solid solutions for highly efficient hydrogen evolution, Adv. Energy Mater. 7 (2017) 1602089.
[31] Daniel Merki, Heron Vrubel, Lorenzo Rovelli, Stéphane Fierro, Xile Hu, Fe, Co, and Ni ions promote the catalytic activity of amorphous molybdenum sulfide films for hydrogen evolution, Chem. Sci. 3 (90 C) (2012) 2515.
[32] Lei Liao, Jie Zhu, Xiaojun Bian, Lina Zhu, Micheál D. Scanlon, Hubert H. Girault, Baohong Liu, MoS2 formed on mesoporous graphene as a highly active catalyst for hydrogen evolution, Adv. Funct. Mater. 23 (42) (2013) 5326–5333.
[33] Honglin Li, Ke Yu, Chao Li, Zheng Tang, Bangjun Guo, Xiang Lei, Hao Fu, Ziqiang Zhu, Charge-transfer induced high efficient hydrogen evolution of MoS_2/graphene cocatalyst, Sci. Rep. 5 (November) (2015) 18730.
[34] Yanguang Li, Hailiang Wang, Liming Xie, Yongye Liang, Guosong Hong, Hongjie Dai, MoS_2 nanoparticles grown on graphene: an advanced catalyst for the hydrogen evolution reaction, J. Am. Chem. Soc. 133 (19) (2011) 7296–7299.

[35] J. Bonde, P. Moses, T. Jaramillo, J. Norskov, I. Chorkendorff, Hydrogen evolution on nano-particulate transition metal sulfides, Faraday Discuss. 140 (2008) 219–231.

[36] Haiqing Zhou, Fang Yu, Yufeng Huang, Jingying Sun, Zhuan Zhu, Robert J. Nielsen, Ran He, Jiming Bao, William A. Goddard III, Shuo Chen, Zhifeng Ren, Efficient hydrogen evolution by ternary molybdenum sulfoselenide particles on self-standing porous nickel diselenide foam, Nat. Commun. 7 (2016) 12765.

[37] Qiufang Gong, Liang Cheng, Changhai Liu, Mei Zhang, Qingliang Feng, Hualin Ye, Min Zeng, Liming Xie, Zhuang Liu, Yanguang Li, Ultrathin MoS_2(1-x)Se_2x alloy nanoflakes for electrocatalytic hydrogen evolution reaction, ACS Catal. 5 (4) (2015) 2213–2219.

[38] Kun Liang, Yong Yan, Limin Guo, Kyle Marcus, Zhao Li, Le Zhou, Yilun Li, Ruquan Ye, Nina Orlovskaya, Yong-Ho Sohn, Yang Yang, Strained $W(Se_xS_{1-x})_2$ nanoporous films for highly efficient hydrogen evolution, ACS Energy Lett. 2 (2017) 1315–1320.

[39] Min-Rui Gao, Jin-Xia Liang, Ya-Rong Zheng, Yun-Fei Xu, Jun Jiang, Qiang Gao, Jun Li, Shu-Hong Yu, An efficient molybdenum disulfide/cobalt diselenide hybrid catalyst for electrochemical hydrogen generation, Nat. Commun. 6 (2015) 5982.

[40] Hongxiu Zhang, Bin Yang, Xiaolin Wu, Zhongjian Li, Lecheng Lei, Xingwang Zhang, Polymorphic $CoSe_2$ with mixed orthorhombic and cubic phases for highly efficient hydrogen evolution reaction, ACS Appl. Mater. Interfaces 7 (3) (2015) 1772–1779.

[41] Qian Liu, Jinle Shi, Jianming Hu, Abdullah M. Asiri, Yonglan Luo, Xuping Sun, $CoSe_2$ nanowires array as a 3D electrode for highly efficient electrochemical hydrogen evolution, ACS Appl. Mater. Interfaces 7 (7) (2015) 3877–3881.

[42] Pengzuo Chen, Kun Xu, Shi Tao, Tianpei Zhou, Yun Tong, Hui Ding, Lidong Zhang, Wangsheng Chu, Changzheng Wu, Yi Xie, Phase-transformation engineering in cobalt diselenide realizing enhanced catalytic activity for hydrogen evolution in an alkaline medium, Adv. Mater. 28 (2016) 7527–7532.

[43] Chuan Xia, Qiu Jiang, Chao Zhao, Mohamed N. Hedhili, Husam N. Alshareef, Selenide-based electrocatalysts and scaffolds for water oxidation applications, Adv. Mater. 28 (1) (2016) 77–85.

[44] Matthew S. Faber, Rafal Dziedzic, Mark A. Lukowski, Nicholas S. Kaiser, Qi Ding, Song Jin, High-performance electrocatalysis using metallic cobalt pyrite (CoS_2) micro- and nanostructures, J. Am. Chem. Soc. 136 (28) (2014) 10053–10061.

[45] E. Nowack, D. Schwarzenbach, Th. Hahn, Charge densities in CoS_2 and NiS_2 (pyrite structure), Acta Crystallograph. Sect. B 47 (5) (1991).

[46] W. Folkerts, G.A. Sawatzky, C. Haas, R.A. de Groot, F.U. Hillebrecht, Electronic structure of some 3D transition-metal pyrites, J. Phys. C: Solid State Phys. 20 (1987) 4135–4144.

[47] R. Yamamoto, A. Machida, Y. Moritomo, A. Nakamura, Reconstruction of the electronic structure in half-metallic CoS_2, Phys. Rev. B 59 (1999) R7793–R7796.

[48] K. Adachi, K. Sato, M. Takeda, Magnetic properties of cobalt and nickel dichalcogenide compounds with pyrite structure, J. Phys. Soc. Jpn. 26 (3) (1969) 631.

[49] T. Goto, Y. Shindo, H. Takahashi, Magnetic properties of the itinerant metamagnetic system $Co(S_{1-x}Se_x)_2$ under high magnetic fields and high pressure, Phys. Rev. B 56 (1997) 14019–14028.

[50] K. Adachi, M. Matsui, M. Kawai, Further investigations on magnetic properties of $Co(S_xSe_{1-x})_2$, J. Phys. Soc. Japan 46 (1979) 1474–1482.

[51] Seo Hyoung Chang, Nemanja Danilovic, Kee-Chul Chang, Ram Subbaraman, Arvydas P. Paulikas, Dillon D. Fong, Matthew J. Highland, Peter M. Baldo, Vojislav R. Stamenkovic, John W. Freeland, Jeffrey a. Eastman, Nenad M. Markovic, Functional links between stability and reactivity of strontium ruthenate single crystals during oxygen evolution, Nat. Commun. 5 (May) (2014) 4191.

[52] Yawei Li, James L. Hart, Mitra L. Taheri, Joshua D. Snyder, Morphological instability in topologically complex, three-dimensional electrocatalytic nanostructures, ACS Catal. 7 (11) (2017) 7995–8005.

[53] Jiahai Wang, Wei Cui, Qian Liu, Zhicai Xing, Abdullah M. Asiri, Xuping Sun, Recent progress in cobalt-based heterogeneous catalysts for electrochemical water splitting, Adv. Mater. 28 (2) (2016) 215–230.

[54] D.A. Chareev, General principles of the synthesis of chalcogenides and pnictides in salt melts using a steady-state temperature gradient, Crystallogr. Rep. 61 (2016) 506–511.

[55] D.A. Chareev, O.S. Volkova, N.V. Geringer, A.V. Koshelev, A.N. Nekrasov, V.O. Osadchii, E.G. Osadchii, O.N. Filimonova, Synthesis of chalcogenide and pnictide crystals in salt melts using a steady-state temperature gradient, Crystallogr. Rep. 61 (4) (2016) 682–691.

[56] N.P. Lyakishev, Phase Diagrams of Binary Metallic Systems, Mashinostroenie, Moscow, Russia, 1996.

[57] Zhi Wei Seh, Kurt D. Fredrickson, Babak Anasori, Jakob Kibsgaard, Alaina L. Strickler, Maria R Lukatskaya, Yury Gogotsi, Thomas F. Jaramillo, Aleksandra Vojvodic, Two-dimensional molybdenum carbide (MXene) as an efficient electrocatalyst for hydrogen evolution, ACS Energy Lett. 1 (2016) 589–594.

[58] Yi-Fan Niu, Jean-Pierre Guin, Tanguy Rouxel, Abdesselam Abdelouas, Johann Troles, Frederic Smektala, Aqueous corrosion of the $GeSe_4$ chalcogenide glass: surface properties and corrosion mechanism, J. Am. Ceram. Soc. 92 (8) (2009) 1779–1787.

[59] Ke Wang, Chongjian Zhou, Dan Xi, Zhongqi Shi, Cheng He, Hongyan Xia, Guiwu Liu, Guanjun Qiao, Component-controllable synthesis of $Co(S_xSe_{1-x})_2$ nanowires supported by carbon fiber paper as high-performance electrode for hydrogen evolution reaction, Nano Energy 18 (2015) 1–11.

[60] Hongju Wang, Dapeng Wu, Kun Cao, Fujuan Wang, Zhiyong Gao, Fang Xu, Kai Jiang, $Co(S_xSe_{1-x})_2$ nanorods arrays with rhombus cross-section exhibiting high catalytic activity for quantum dot sensitized solar cells, Electrochim. Acta 251 (2017) 378–387.

[61] Ling Fang, Wenxiang Li, Yongxin Guan, Yangyang Feng, Huijuan Zhang, Shilong Wang, Yu Wang, Tuning unique peapod-like $Co(S_xSe_{1-x})_2$ nanoparticles for efficient overall water splitting, Adv. Funct. Mater. 27 (2017) 1701008.

[62] Jingyan Zhang, Wen Xiao, Pinxian Xi, Shibo Xi, Yonghua Du, Daqiang Gao, Jun Ding, Activating and optimizing activity of CoS_2 for hydrogen evolution reaction through the synergic effect of N dopants and S vacancies, ACS Energy Lett. 2 (5) (2017) 1022–1028.

[63] Youwen Liu, Xuemin Hua, Chong Xiao, Tengfei Zhou, Pengcheng Huang, Zaiping Guo, Bicai Pan, Yi Xie, Heterogeneous spin states in ultrathin nanosheets induce subtle lattice distortion to trigger efficient hydrogen evolution, J. Am. Chem. Soc. 138 (15) (2016) 5087–5092.

[64] Nenad M. Markovic, Stella T. Sarraf, Hubert a. Gasteiger, Philip N. Ross, Temperature-dependent hydrogen electrochemistry on platinum low-index single crystal surfaces in acid solutions, J. Phys. Chem. B 101 (1997) 5405–5413.

[65] Tatsuya Shinagawa, Angel T. Garcia-Esparza, Kazuhiro Takanabe, Insight on Tafel slopes from a microkinetic analysis of aqueous electrocatalysis for energy conversion, Sci. Rep. 5 (2015) 13801.

[66] B.E. Conway, B.V. Tilak, Interfacial processes involving electrocatalytic evolution and oxidation of H2, and the role of chemisorbed H, Electrochim. Acta 47 (22–23) (2002) 3571–3594.

[67] B. Conway, Behavior and characterization of kinetically involved chemisorbed intermediates in electrocatalysis of gas evolution reactions, Adv. Catal. 38 (1992) 1–147.

[68] D.R. Lide, CRC Handbook of Chemistry and Physics, 89th ed., CRC Press, Boca Raton, FL, 2008.

[69] Q. Jia, J. Li, K. Caldwell, D. Ramaker, J. Ziegelbauer, R. Kukreja, A. Kongkanand, S. Mukerjee, Circumventing metal dissolution-induced degradation of pt-alloy catalysts in proton exchange membrane fuel cells: revealing the asymmetric volcano nature of redox catalysis, ACS Catal. 6 (2016) 928–938.

[70] Haichuan Zhang, Yingjie Li, Guoxin Zhang, Tianhao Xu, Pengbo Wan, Xiaoming Sun, A metallic CoS2 nanopyramid array grown on 3D carbon fiber paper as an excellent electrocatalyst for hydrogen evolution, J. Mater. Chem. A 3 (12) (2015) 6306–6310.

[71] S. Karthe, R. Szargan, E. Suoninen, Oxidation of pyrite surfaces: a photoelectron spectroscopic study, Appl. Surf. Sci. 72 (2) (1993) 157–170.

[72] I. Uhlig, R. Szargan, H.W. Nesbitt, K. Laajalehto, Surface states and reactivity of pyrite and marcasite, Appl. Surf. Sci. 179 (1–4) (2001) 222–229.

[73] H. van der Heide, R. Hemmel, C.F. van Bruggen, C. Haas, X-ray photoelectron spectra of 3d transition metal pyrites, J. Solid State Chem. 33 (1) (1980) 17–25.

[74] L. Zhu, D. Susac, M. Teo, K.C. Wong, P.C. Wong, R.R. Parsons, D. Bizzotto, K.A.R. Mitchell, S.A. Campbell, Investigation of CoS_2-based thin films as model catalysts for the oxygen reduction reaction, J. Catal. 258 (1) (2008) 235–242.

[75] Pascale Bonnissel-Gissinger, Marc Alnot, Jean Jacques Ehrhardt, Philippe Behra, Surface oxidation of pyrite as a function of pH, Environ. Sci. Technol. 32 (19) (1998) 2839–2845.

[76] J.C. Muijsers, T. Weber, R.M. Vanhardeveld, H.W. Zandbergen, J.W. Niemantsverdriet, Sulfidation study of molybdenum oxide using MoO_3/SiO_2/Si(100) model catalysts and Mo-IV3-sulfur cluster compounds, J. Catal. 157 (1995) 698–705.

[77] Zhebo Chen, Dustin Cummins, Benjamin N. Reinecke, Ezra Clark, Mahendra K. Sunkara, Thomas F. Jaramillo, Core-shell MoO_3-MoS_2 nanowires for hydrogen evolution: a functional design for electrocatalytic materials, Nano Lett. 11 (10) (2011) 4168–4175.

[78] Heron Vrubel, Daniel Merki, Xile Hu, Hydrogen evolution catalyzed by MoS_3 and MoS_2 particles, Energy Environ. Sci. 5 (3) (2012) 6136–6144.

[79] Hernan G. Sanchez Casalongue, Jesse D. Benck, Charlie Tsai, Rasmus K.B. Karlsson, Sarp Kaya, May Ling Ng, Lars G.M. Pettersson, Frank Abild-Pedersen, J.K. Nørskov, Hirohito Ogasawara, Thomas F. Jaramillo, Anders Nilsson, Operando characterization of an amorphous molybdenum sulfide nanoparticle catalyst during the hydrogen evolution reaction, J. Phys. Chem. C 118 (50) (2014) 29252–29259.

[80] Mark C. Biesinger, Brad P. Payne, Andrew P. Grosvenor, Leo W.M. Lau, Andrea R. Gerson, Roger St C. Smart, Resolving surface chemical states in XPS analysis of first row transition metals, oxides and hydroxides: Cr, Mn, Fe, Co and Ni, Appl. Surf. Sci. 257 (7) (2011) 2717–2730.

[81] D.C. Higgins, F.M. Hassan, M.H. Seo, J.Y. Choi, M.A. Hoque, D.U. Lee, Z. Chen, Shape-controlled octahedral cobalt disulfide nanoparticles supported on nitrogen and sulfur-doped graphene/carbon nanotube composites for oxygen reduction in acidic electrolyte, J. Mater. Chem. A 3 (12) (2015) 6340–6350.

[82] J. Yang, H. Liu, W. Martens, R. Frost, Synthesis and characterization of cobalt hydroxide, cobalt oxyhydroxide, and cobalt oxide nanodiscs, J. Phys. Chem. C 114 (7) (2010) 111–119.

[83] Annette Foelske, Hans Henning Strehblow, Passivity of cobalt in borate buffer at pH 9.3 studied by X-ray photoelectron spectroscopy, Surf. Interface Anal. 29 (8) (2000) 548–555.

[84] Charlie Tsai, Karen Chan, Frank Abild-Pedersen, Jens K. Nørskov, Active edge sites in $MoSe_2$ and WSe_2 catalysts for the hydrogen evolution reaction: a density functional study, PCCP 16 (26) (2014) 13156–13164.